2

Study of Ferromagnet-Antiferromagnet Interfaces Using X-Ray PEEM

A. Scholl, H. Ohldag, F. Nolting, S. Anders, and J. Stöhr

This chapter discusses polarization dependent X-ray photoemission electron microscopy (X-PEEM) and its application to coupled magnetic layers, in particular ferromagnet-antiferromagnet structures.

2.1 Introduction

Over the last decades, magnetism has evolved into one of the cornerstones of information storage technology, providing the foundation of a $50 billion dollar per year worldwide storage business. Today's high-tech magnetic devices are based on thin films, often patterned into sub-micron sized cells, and rely on the existence of magnetically well-defined states. Over the last ten years, our understanding of the structure and properties of magnetic thin films and multilayers has progressed remarkably, yet one key problem in our understanding has remained, namely, the characterization and understanding of interfaces, omnipresent in modern magnetic structures. Many of today's forefront areas in magnetism require a better understanding of the spin structure at interfaces [1, 2]. Examples are giant magnetoresistance structures and spin tunnel junctions [3], as well as "spintronics" devices based on spin injection into a semiconductor [4, 5]. In these structures, spin transport across metal-metal, metal-oxide, metal-semiconductor, and semiconductor-semiconductor interfaces is believed to strongly depend on the magnetic properties of the interfaces.

Today's magneto-electronic devices typically contain ferro-, ferri-, and antiferromagnetic layers, and the characterization of their complex structure requires new experimental tools that are sensitive to all three flavors of magnetic order. While there are numerous techniques sensitive to ferromagnetic order in thin-film systems ranging from magnetic force microscopy, over the magneto-optical Kerr effect, to photoemission techniques, there is clearly a need for methods that are also sensitive to antiferromagnetic order. The determination of the electronic, chemical, or magnetic structure of interfaces is especially challenging, since the weak signal originating from the interface has to be detected and isolated from the large background of the

bulk. For lack of better capabilities scientists have tried to circumvent this problem by studying the early stages of interface formation with surface science techniques, by investigating ultrathin model systems, or by studying simply the "bulk" materials forming the interface. Unsubstantiated assumptions are often made in the interpretation of experimental data or for model calculations about the existence of bulk-like structures all the way to the interface or about the existence of atomically abrupt interfaces without chemical intermixing or roughness. In this article, we shall show that in reality interfaces are quite different.

Here, we present the investigation of a specific interface problem that is of considerable scientific interest and technological importance: the unsolved origin of exchange bias in antiferromagnet-ferromagnet sandwiches [6,7]. Discovered in 1956 by Meiklejohn and Bean [8], exchange bias refers to the unidirectional pinning of a ferromagnetic layer by an adjacent antiferromagnet. Ferromagnetic films typically have a preferred magnetization axis, "easy axis," and the spins prefer to align along this axis. There are two equally stable easy spin directions (rotated by 180°) along this axis, and it costs the same energy and requires the same external field to align the spins along either easy direction. When a ferromagnet (FM) is grown on an antiferromagnet (AFM), the exchange coupling between the two systems leads to an increased coercivity of the ferromagnet. This is usually attributed to an increased interface anisotropy, resulting from the coupling of "interface moments" to the antiferromagnet. The ferromagnetic hysteresis loop is still symmetric, indicating two equivalent easy directions. If, on the other hand, the AFM-FM system is grown in a magnetic field or after growth annealed in a magnetic field to temperatures above the AFM Néel temperature, the hysteresis loop becomes asymmetric and is shifted from zero by a field $\mathbf{H}_{\mathrm{B}}$. This unidirectional shift is called exchange bias and reflects the fact that there is now a preferred easy magnetization *direction* for the FM. The ferromagnet is pinned by the antiferromagnet into this easy direction, which is opposite to the bias field direction H_{B}. The fact that the origin of the exchange bias effect is still hotly debated after more than forty years of research is due to the difficulty associated with determining the magnetic interfacial structure mentioned above. While there is little doubt about the crucial importance of the interfacial spin structure, and more specifically about the existence of uncompensated "interfacial spins" that give rise to the exchange bias phenomenon [9], two fundamental problems have prevented a solution of the puzzle.

The first is the difficulty of imaging the microscopic antiferromagnetic structure in thin films with conventional techniques. While the AFM domain structure in bulk single crystals has been studied since the late 1950s [10–12], little is known about the domain structure in thin films. For example, in well-annealed bulk NiO, the typical domain size is in the 0.1–1 mm range [10, 13] whereas in epitaxial NiO films, the domain size has been estimated to be less than 50 nm [14]. This size is below the spatial resolution of neutron diffraction topography (about 70 μm), X-ray diffraction topography (1–2 μm) [10], and of conventional [10,13] and nonlinear [15,16] optical techniques, which are limited by diffraction (about 0.2 μm). On a microscopic level, the exchange coupling across the AFM-FM interface is expected to proceed domain by

domain, leading to a correlation of the AFM with the FM domain structure. Therefore, measurement of the antiferromagnetic domain structure is of crucial importance.

The second problem is the determination of the interfacial spin structure and its relationship with the magnetic structure in the AFM and FM films. Still little is known about the origin of uncompensated interfacial spins and their role in the observed coercivity increase and the exchange bias effect. Previous models have invoked statistical arguments for the existence of uncompensated interfacial spins. These models take into account one or more of the following aspects: uncompensated termination of bulk antiferromagnetic domains [9], spin-flop canting of antiferromagnetic spins [17], and interface and bulk defects [18, 19]. It has also been proposed that coercivity and bias arise from different mechanisms like canting and defects, respectively [18].

The present chapter takes a new look at an old problem, utilizing X-ray spectroscopy and microscopy methods that have only recently been developed. The spectromicroscopy approach, utilized here, combines two well-established concepts, polarized X-ray absorption spectroscopy (XAS) and electron microscopy [20, 21]. It has many key strengths needed ultimately to solve the exchange bias puzzle. Because of the elemental and chemical specificity of XAS, one can tune into specific layers by tuning the photon energy. X-ray polarization control opens the door for magnetic studies by using X-ray magnetic linear dichroism (XMLD) [22–26] on antiferromagnets, and X-ray magnetic circular dichroism (XMCD) [27–29] on ferro- and ferrimagnets. Electron yield detection provides limited sampling depth [20, 30], and for thin film sandwiches, the signal contains a sizeable interface contribution. An electron microscope, in our case detecting the secondary photoelectrons that are emitted after X-ray absorption, offers high spatial resolution.

This chapter first reviews the concepts of XMLD and XMCD spectroscopies and photoemission electron microscopy (PEEM). It then gives experimental details on polarization control and the present PEEM-2 microscope at the Advanced Light Source (ALS) in Berkeley, U.S.A. Experimental results are discussed next for the structure of selected antiferromagnetic surfaces and for their coupling to ferromagnetic overlayers. Finally, a summary and outlook are given.

2.2 Photoemission Electron Microscopy

X-ray magnetic circular dichroism, which was first observed at the Fe K edge in 1987 [27], is today a standard method for the study of magnetic thin films and surfaces [1]. The availability of polarized and tunable X-rays from today's brilliant synchrotron sources has played an important role in the success of X-ray dichroism techniques. The last ten years have seen great progress following the first XMCD spectroscopy measurements at the important transition metal L edges [28] and the first XMCD microscopy experiments [31]. Although called "photoemission electron microscopy", PEEM is actually an X-ray absorption technique, since contrast is generated by lateral variations in the X-ray absorption crosssection. Since PEEM is based on the absorption of X-rays in matter, we will first discuss X-ray absorption spectroscopy in general. We will furthermore only discuss the near edge structure

within a few eV of the absorption edge, because it contains the information about the chemical and magnetic properties of the sample in which we are interested. A general overview of near edge X-ray absorption techniques can be found in [32], and XMCD spectroscopy has been reviewed in [29, 33]. We will only briefly discuss X-ray absorption measurements in ferromagnets, and we refer the reader to the contribution by W. Kuch for detailed description of the PEEM technique applied to ferromagnets (Chap. 1 of this book).

2.2.1 X-Ray Absorption Spectroscopy

X-ray absorption spectroscopy (XAS) utilizes the energy-dependent absorption of X-rays to obtain information about the elemental composition of the sample, the chemical environment of its constituents, and its magnetic structure. Core electrons are excited in the absorption process into empty states above the Fermi energy and thereby probe the electronic and magnetic properties of the empty valence levels. X-ray transmission detection and electron yield detection are the most commonly used methods for measuring the absorption coefficient μ as a function of the photon energy E, and can both be used in X-ray microscopes. Transmission microscopes provide direct quantitative access to the spatial distribution of $\mu(E)$, but require samples sufficiently thin to be penetrated by X-rays [34]. The absorption length in $3d$ transition metals in the soft X-ray region is typically about 20–100 nm [30, 35]. An advantage of X-ray detection techniques is their insensitivity to external magnetic fields.

Electron yield detection techniques like PEEM measure the absorption coefficient indirectly, collecting the emitted secondary electrons generated in the electron cascade that follows the creation of the primary core hole in the absorption process. The total electron yield is proportional to the number of absorbed photons in a near surface region of the sample whose depth is given by the mean free path of the low energy secondary electrons. The probing depth of electron yield detection is typically a few nanometers [30]. This is much smaller than the X-ray penetration length, which explains the surface sensitivity of PEEM [36]. After correction of saturation effects caused by the finite X-ray penetration depth, and the application of suitable normalization and background subtraction procedures, the absorption coefficient can be extracted from the yield spectrum [37, 38]. The difficulty of imaging magnetic structures in external applied fields can be overcome by using very localized fields generated by micro-coils.

The $L(2p)$ X-ray absorption spectrum of transition metal oxides such as NiO, CoO, and $LaFeO_3$ is dominated by the large spin-orbit splitting of the core level electronic $2p_{3/2}$ and $2p_{1/2}$ states, which is on the order of 15 eV. An example of an XAS spectrum at the Fe edge of a $LaFeO_3$ sample measured by electron yield detection is shown in Fig. 2.1. Dipole selection rules only permit transitions from the $2p$ states into $4s$ or $3d$ valence states, and the excitation into the narrow $3d$ states is responsible for the strong resonances. The fine structure of the resonance is caused by two effects, (i) the electron correlation due to the electron-electron interaction in the initial and final states of the absorption process and (ii) the crystal field interaction.

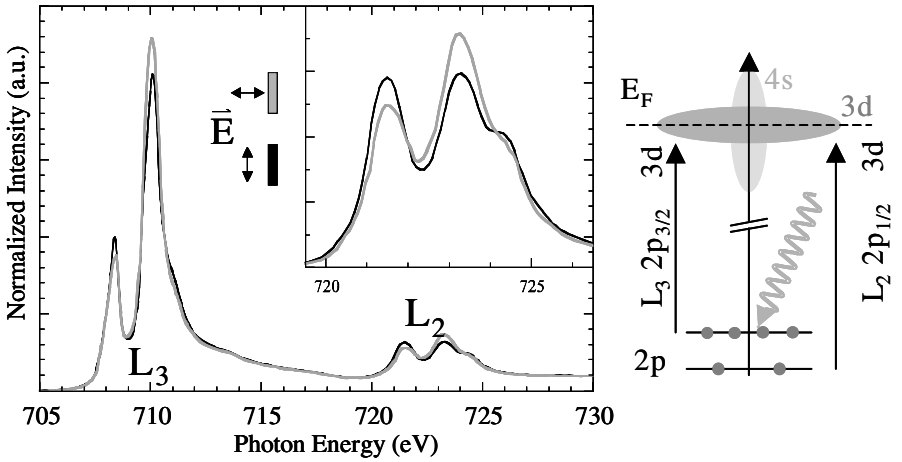

Fig. 2.1. X-ray absorption spectra of antiferromagnetic $LaFeO_3$ (001) measured with the linear X-ray polarization parallel to the sample (black) and perpendicular to the sample (gray). The spectra are corrected for electron yield saturation effects and for the finite linear polarization (80%) of the original spectra. The spectrum for $\vec{E}$ perpendicular to the surface, corresponding to an unphysical grazing X-ray incidence of 0°, has been derived from angle-dependent spectra. The spectra were measured with no spatial resolution on a large sample area. Strong X-ray magnetic linear dichroism (XMLD) appears at the multiplet split L_3 and L_2 edges. The X-ray absorption process is described on the right

Both effects are of comparable size ($\sim$ 1 eV), causing the complex structure of oxide spectra. These effects split the absorption resonances into multiplets.

2.2.2 X-Ray Magnetic Linear Dichroism (XMLD)

Magnetic effects become apparent in the absorption spectrum when linearly polarized X-rays are used [22–26]. A change in the X-ray polarization causes a change in the line strength of multiplet lines depending on the angular momentum character of the corresponding initial and final states. Since usually many multiplet lines are superimposed in an absorption spectrum, only a net effect is observable, which depends on the angle between the direction of the X-ray polarization vector and the axis of the magnetization. Thus, the ingredients for a strong magnetic linear dichroism in XAS are a strong spin-orbit interaction of the core level and a well resolved multiplet structure in the absorption resonance. In transition metal oxides, both conditions are fulfilled, leading to a significant polarization-dependent magnetic contribution to the intensity of multiplet lines in XAS. This effect is called X-ray magnetic linear dichroism (XMLD). Linearly polarized X-rays probe the angle α between the linear X-ray polarization vector $\vec{E}$ and the orientation of the magnetization axis $\vec{A}$. The angle and magnetization dependence of the XMLD intensity is then given by: $I_{\mathrm{XLMD}} \sim (1 - 3\cos^2\alpha)\langle M^2\rangle_T$. Here $\langle M^2\rangle_T$ is the statistical average of the squared local magnetization at the temperature T. Contributions linear in M vanish because of

the compensated magnetic structure and the zero macroscopic magnetic moment of antiferromagnets. Antiferromagnets, therefore, do not show X-ray magnetic circular dichroism.

The two polarization-dependent absorption spectra in Fig. 2.1 were measured on an antiferromagnetically ordered $LaFeO_3$ thin film, grown on $SrTiO_3(001)$, with the linear X-ray polarization lying parallel to (black) and perpendicular to (gray) the sample surface. The spectra were acquired without spatial resolution and, thus, average over a large sample area. Analysis of the polarization and angular dependence of the XMLD effect in absorption spectra allows the determination of the average direction of the magnetic axis. It is known from multiplet calculations that a higher 2nd peak at the L_3 and the L_2 resonances indicates a more parallel orientation of the magnetic axis $\vec{A}$ and the X-ray polarization $\vec{E}$ in the three antiferromagnetic oxides α-Fe_2O_3 [25], NiO [26], and CoO. The magnetic Fe atom in $LaFeO_3$ sits in an identical local crystallographic environment as in α-Fe_2O_3 and, therefore, has the same multiplet absorption structure and a similar XMLD signature. The spectra show that $\vec{A}$ is closer, on average, to the out-of-plane polarization direction than to the in-plane polarization direction, because the second peak is higher in the out-of-plane spectrum (gray line). By rotating the sample around the surface normal, we can furthermore determine the macroscopic in-plane symmetry of the system, which is fourfold in $LaFeO_3(001)$ [38, 39].

2.2.3 X-Ray Magnetic Circular Dichroism (XMCD)

The interaction of circularly polarized X-rays with a ferromagnetically ordered sample, and its application for quantitative magnetization mapping with X-ray PEEM, are discussed in detail by W. Kuch (Chap. 1 of this book). Circularly polarized X-rays probe the direction of the atomic magnetic moment in a ferromagnet. The angle and magnetization dependence of X-ray magnetic circular dichroism in the total absorption signal is given by $I_{\mathrm{XMCD}} \sim \cos\alpha\langle M\rangle_T$, with α denoting the angle between the X-ray helicity vector $\vec{\sigma}$ (parallel to the X-ray propagation direction) and the magnetization $\vec{M}$. Strong XMCD effects of opposite sign appear at the L_3 and L_2 $2p \rightarrow 3d$ resonances of the transition metal ferromagnets Fe, Co, and Ni.

2.2.4 Temperature Dependence of X-Ray Magnetic Dichroism

In contrast to ferromagnets, the spin direction in an antiferromagnet cannot be easily switched or rotated. The characteristic temperature dependence of the XMLD signal is therefore the most direct experimental proof that a feature in the absorption spectrum is of magnetic origin. Let us first consider the simpler case of XMCD. As a first order effect, the contribution of XMCD to the total absorption is directly proportional to the macroscopic magnetization $\langle M\rangle_T$. In mean field approximation the statistical average of the magnetization per atom in units of the electron moment $g\mu_B$ is given by $\langle M\rangle_T = JB_J(x)$, with J the spin moment of the magnetic d-shell and $x = H(M)/kT$. We have neglected the contribution of the orbital moment, which is usually strongly

quenched in solids due to the crystal field. $H(M)$ is the molecular field, or Weiss field, generated by the magnetization M, and $B_J(x) = \frac{2J+1}{2J} \coth\left(\frac{2J+1}{2J}x\right) - \frac{1}{2J} \coth\left(\frac{1}{2J}x\right)$ is the Brillouin function. This implicit equation can be numerically evaluated as a function of T. The temperature dependence of XMLD is slightly more complex, because $\langle M^2 \rangle_T$ has to be evaluated [22, 26, 39]. A numerical solution for a given J is possible using the identity $\langle M^2 \rangle = J(J+1) - \langle M \rangle \coth(x/2)$. This formula can again be numerically evaluated using the mean field expression for $\langle M \rangle_T$ and $x = H(M)/kT$. We will later use this expression to describe the temperature dependence of the XMLD contrast in the antiferromagnet $LaFeO_3$.

2.2.5 Experiment

Photoemission electron microscopy utilizes local variations in electron emission, and, therefore, the local X-ray absorption, in order to generate image contrast. The electrons emitted from the sample are accelerated by a strong electric field (typically 15–20 kV) toward the electron optical column, which forms a magnified image of the local electron yield. PEEM is a parallel imaging technique, and the spatial resolution is solely determined by the resolution of the electron optics, while the intensity is proportional to the X-ray flux density. The electron optical column contains typically two or more electrostatic or magnetic electron lenses, corrector elements such as a stigmator and deflector, an angle-limiting aperture in the backfocal plane of one of the lenses, and a detector (a fluorescent screen or a multichannel plate detector that is imaged by a CCD camera). A schematic drawing of the PEEM-2 facility, located at the Advanced Light Source, is shown in Fig. 2.2.

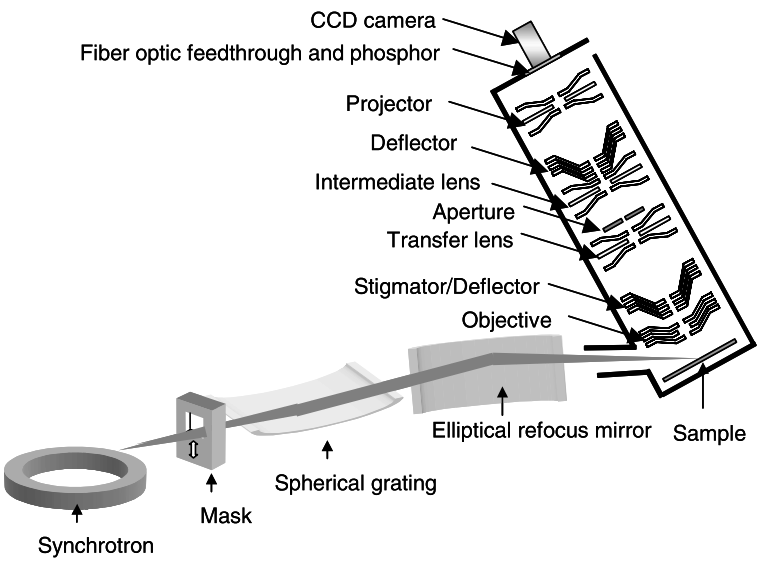

Fig. 2.2. Layout of beamline 7.3.1.1 at the Advanced Light Source and PEEM-2 endstation

An X-ray source providing radiation with tunable energy and variable polarization from left and right circular to linear is essential for the investigation of magnetic materials [29]. The PEEM-2 instrument uses bending magnet radiation. The polarization is selected by moving a mask vertically in the beam. Radiation in the plane of the storage ring is linearly polarized, while above and below the plane the radiation is right and left circularly polarized. The radiation is monochromatized using a spherical grating monochromator and focused onto the sample using an elliptical refocusing mirror. The sample is at high negative potential for this design, and electrons emitted from the sample are imaged using an all-electrostatic four-lens electron optical system [36]. A stigmator-deflector assembly in the backfocal plane of the objective lens and an additional deflector behind the intermediate lens correct for machining and for alignment errors of the lenses. The angle-defining aperture is located in the backfocal plane of the transfer lens.

The best spatial resolution with PEEM instruments is achieved using UV radiation with an excitation energy that just exceeds the work function. The narrow energy distribution of the threshold photoelectrons of 0.1–1 eV minimizes chromatic image errors. A resolution of below 10 nm, close to the theoretical limit of 5 nm, has been

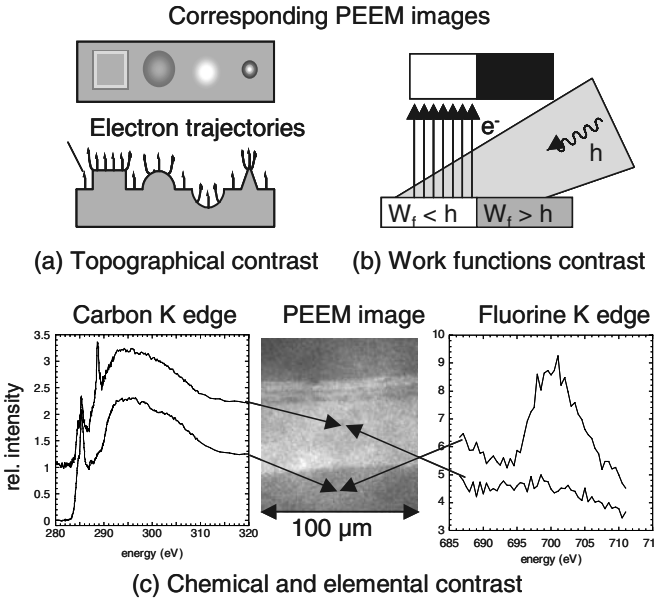

Fig. 2.3. PEEM contrast mechanisms. (**a**) Topographic contrast caused by surface features. (**b**) Work function contrast caused by work function changes that affect the electron yield intensity from different regions. (**c**) Examples for chemical and elemental contrast. The PEEM image in the middle, which was acquired at 280 eV (contrast is mostly topographical), shows a wear track on a computer hard disk lubricated with fluorocarbon [21]. To the left and right, local absorption spectra are shown. The additional peak in the carbon spectrum (288.5 eV) in the wear track indicates oxidation of the carbon. The fluorine spectra show removal of fluorine in the wear track. Both are signatures of lubricant degradation

achieved [40]. If X-rays are used as the excitation source, the emitted electrons are mainly secondary electrons with a substantially wider energy distribution of about 5 eV [41] that leads to a strong increase in chromatic aberrations and a deterioration of the spatial resolution. The highest spatial resolution obtained with X-rays today is in the 20 nm range [36, 42, 43], and for magnetic imaging more typically in the 50–100 nm range.

PEEM relies on several mechanisms for image contrast. Topographic contrast is caused by distortions of the accelerating electric field at topographic surface features. Local changes in work function, for example, caused by different materials, result in changes in the electron yield and, therefore, lead to image contrast. Work function contrast is particularly strong for excitation with UV, depending on whether the UV energy is above or below the work function of the illuminated sample area. These two contrast mechanisms are illustrated in Fig. 2.3a and b. The combination of PEEM and tunable synchrotron radiation adds elemental and chemical contrast by utilizing the sensitivity of the near edge absorption structure to the chemical environment of an atom. Elemental and chemical contrast are explained in Fig. 2.3c. Through the use of XMCD and XMLD magnetic dichroism techniques, it is possible to obtain ferro- and antiferromagnetic contrast, respectively.

2.3 Antiferromagnetic Structure of $LaFeO_3$ Thin Films

We will start our discussion of domain imaging of antiferromagnets with measurements on $LaFeO_3$(001) thin films [39, 44]. These are, to our knowledge, the first measurements showing the magnetic microstructure of an antiferromagnetic thin film. The thin $LaFeO_3$ films were grown by molecular beam epitaxy (MBE) on $SrTiO_3$(001) substrates and were characterized by X-ray diffraction and transmission electron microscopy (TEM). The orthorhombic $LaFeO_3$ layer forms $\sim$ 100-nm-sized crystallographic twins with orthogonal, in-plane c-axes along the cubic [100] and [010] axes of the substrate. The sample geometry is sketched in Fig. 2.4. PEEM images acquired at energies close to the Fe L_3 edge show a variation in image contrast, which is a result of the magnetic domain structure of the film. The images were acquired with the linear X-ray polarization vector $\vec{E}$ in the sample plane and parallel to the [100] direction of the cubic $SrTiO_3$ substrate. In this geometry, PEEM is sensitive to the angle between the in-plane projection of the magnetic axis $\vec{A}$ and the polarization $\vec{E}$.

The depicted images represent a subset of a series of images, an image stack, acquired at consecutive X-ray energies. An image stack contains data for a pixel-by-pixel calculation of local X-ray absorption spectra. Exemplary spectra from two regions are shown at the bottom of Fig. 2.4. Two representative regions of reversed contrast are marked in the images by gray and black bordering. The spectra were generated by plotting the local image intensity as a function of the energy of the incident X-rays. A comparison with the spatially averaged, angular resolved spectra in Fig. 2.1 reveals the magnetic origin of the intensity variation in the local PEEM spectra. The higher intensity of the higher-energy L_2 and L_3 multiplet lines in the

dotted-line spectrum indicates a more parallel alignment of $\vec{A}$ and $\vec{E}$ in the gray-bordered area than in the black-bordered area. The PEEM images at energy positions 1 and 7 show no image contrast, demonstrating the chemical homogeneity (no elemental contrast above edge) and smoothness (no topographic contrast below edge) of the sample. However, at three particular energies, corresponding to the main Fe multiplet lines, an image contrast of alternating sign appears that is of magnetic origin (images 2, 4, and 6).

We usually apply a normalization procedure in order to suppress nonmagnetic contrast, such as elemental or topographical contrast, and to correct for the inhomogeneity in the sample illumination. We start with two PEEM images that exhibit strong but opposite XMLD contrast, e.g., images 2 and 4 in Fig. 2.4 or alternatively images A and B in Fig. 2.5, acquired at energies $E_A = 721.5\,\text{eV}$ and $E_B = 723.2\,\text{eV}$. The approximately equal intensity of the multiplet lines A and B at the Fe L_2 edge usually improves the suppression of nonmagnetic contrast. An image exhibiting enhanced magnetic contrast is derived by calculating the ratio image B/A or the asymmetry image $(B-A)/(B+A)$. If the magnetic contribution is significantly smaller than the total image intensity, then ratio and asymmetry images are equivalent except for a linear transformation. This condition is usually fulfilled (see Fig. 2.4). We refer to the

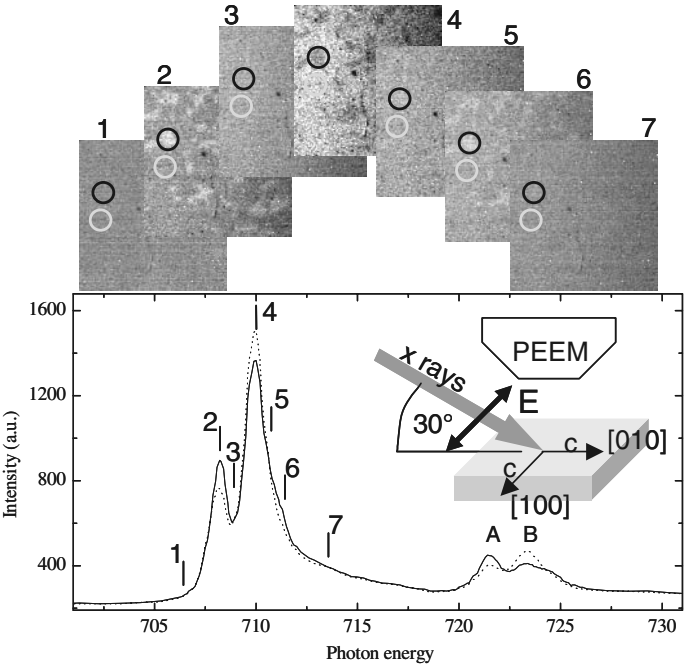

Fig. 2.4. PEEM images (top) and local XMLD spectra (bottom) of a thin $LaFeO_3(001)$ film. The measurement geometry is shown in the inset. The photon energies at which PEEM images were acquired are marked by short vertical lines. Circles mark magnetic domains, which appear with opposite contrast in the images

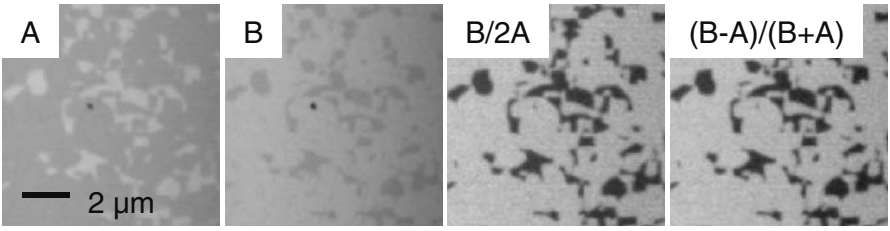

Fig. 2.5. PEEM images for $LaFeO_3(001)$ acquired at the Fe L_2 edge at $E_A = 721.5$ eV and $E_B = 723.2$ eV. The magnetic contrast is enhanced in the ratio (B/A) and the asymmetry image $(B - A)/(B + A)$

ratio image as the *XMLD image*. Its contrast is a measure for the spatial variation of $\langle M^2 \rangle_T$ and for the local angle α between the magnetic axis and the X-ray polarization vector. On $LaFeO_3$ a higher intensity in the XMLD image indicates a more parallel alignment of $\vec{A}$ and $\vec{E}$ and a lower intensity a more perpendicular alignment. The regions of different brightness, therefore, represent magnetic domains with different orientations of the antiferromagnetic axis, assuming a constant moment.

The magnetic origin of the contrast can be verified by studying its temperature dependence (see above). A selection of images acquired at increasing temperatures is shown in Fig. 2.6. Approaching the Néel temperature of the film, which is 740 K in bulk $LaFeO_3$, the image contrast starts to disappear and, as expected for a magnetic effect, fully reappears after cooling down to room temperature. In Fig. 2.6, the decreasing XMLD contrast, referenced to 0 K, is displayed as a function of temperature. The match between the two temperature cycles and the preserved XMLD signal after the return to room temperature demonstrate the chemical stability of the sample upon heating. The continuous curve in Fig. 2.6 shows the mean field fit for $\langle M^2 \rangle_T$ using $J = 5/2$, appropriately shifted and scaled to fit the data. The curve apparently describes the data accurately, giving further evidence for the magnetic origin of the image contrast. Extrapolation of the curve to zero XMLD signal yields a magnetic transition temperature of 670 K, well below the bulk Néel temperature of 740 K, which is marked by an arrow in the plot. We attribute this reduced transition temperature to epitaxial strain in the film modifying the bonding angles and bonding distances, thereby affecting the strength of the Fe-O-Fe superexchange responsible for the magnetic interaction in the system. The absolute error in the temperature measurement is approximately 10 K, as checked by referencing two thermocouple pairs to each other.

The question arises why domains form in an antiferromagnet. Domain formation in antiferromagnets, as in ferromagnets, is expected to result from a process of energy minimization. The main contributors to the magnetic energy of a magnetic system are the exchange energy (which aligns neighboring moments), the dipolar energy (which favors flux closure), the spin-orbit energy, which gives rise to the magneto-crystalline anisotropy (and favors a spin orientation along an "easy" crystallographic axis), and a magneto-elastic term (which favors a certain spin orientation relative to

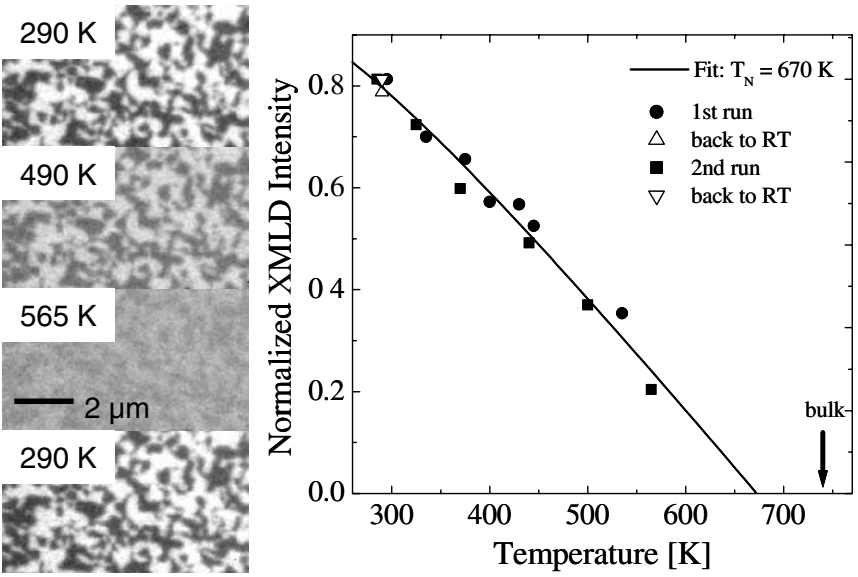

Fig. 2.6. Temperature dependence of XMLD contrast for $LaFeO_3$(001). The contrast disappears approaching the Néel temperature of $LaFeO_3$ (bulk: 740 K). The XMLD intensity measured in two temperature cycles is plotted as a function of temperature and fitted with the expression of in mean field theory using a reduced $T_N = 670$ K

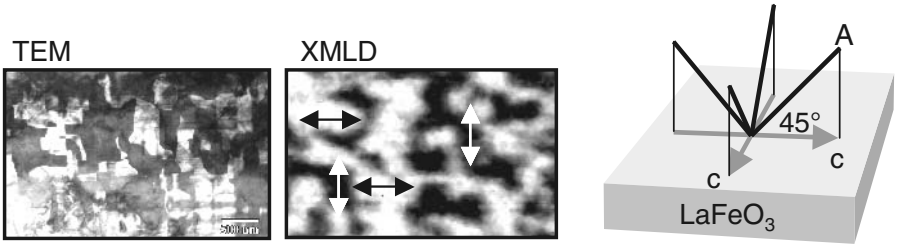

Fig. 2.7. Crystallographic and magnetic structure of LaFeO3(001), in comparison. The contrast in the TEM image (*left*) results from crystallographic twin domains with a horizontal (white domains) and vertical (black domains) c-axis. The XMLD contrast originates from antiferromagnetic domains with horizontal (*white*) and vertical (*black*) in-plane projection of *A*. Both images were obtained from the same sample, but from different regions, so no one-to-one correspondence exists. The directions of A in relation to the c-axes of the twin domains are shown on the *right*

the strain axis). Unlike in ferromagnets, dipolar effects play a negligible role in *bulk* antiferromagnets, because of their vanishing macroscopic magnetization. However, in two-dimensional antiferromagnets, one may have a competition between dipole-dipole and magnetic anisotropy energies, with the former favoring spin alignment perpendicular to the plane [45].

In practice, the antiferromagnetic domain configuration and the local orientation of the antiferromagnetic axis are typically determined by the local crystallographic structure, including defects, and the local crystal strain. Some domain configurations, while not representing global free-energy minima, may still be meta-stable [46]. A four-wall (four T domains) configuration in NiO is such a configuration [47]. Finally, in a perfect crystal, the lowering of the free energy accompanying an increase in entropy can lead to an equilibrium multidomain structure. An example are S-domain walls in NiO, where a multidomain configuration is thermodynamically favored [48] over a large temperature range [49].

The orthorhombic $LaFeO_3$ film, grown on cubic $SrTiO_3(001)$, forms crystallographic twin domains exhibiting orthogonal, in-plane c-axes. These twins are responsible for the black and white contrast in the TEM image, shown on the left in Fig. 2.7. Comparison of the crystallographic structure with XMLD images of the magnetic structure obtained by PEEM (center) reveals a clear similarity in the patterns, which show structures of comparable shape and size. The TEM and XMLD images were acquired on the same sample, but at a different sample position. The correspondence between the patterns demonstrates that the magnetic domain configuration in $LaFeO_3$is indeed dominated by crystallography. The directions of the antiferromagnetic axes $\vec{A}$ and the crystallographic c-axes of the twin domains, determined from TEM and XMLD microscopy in conjunction with X-ray diffraction and XMLD spectroscopy data, are shown on the right in Fig. 2.7.

2.4 Exchange Coupling at the Co/NiO(001) Interface

The magnetic structure at the interface of magnetic layers influences and controls their magnetic interaction and, therefore, has to be known in order to understand interface phenomena such as exchange bias. PEEM is capable of imaging the antiferromagnetic domain structure, as shown above. Polarization-dependent measurements, furthermore, allow us to quantify the local orientation of the spin directions in ferromagnets and antiferromagnets in three dimensions. In the following, we shall illustrate these capabilities by PEEM studies on 10–20 Å thick Co layers grown on the (001) surface of NiO single crystals.

NiO is often used as the AFM in practical exchange bias structures and, over the years, has served as a valuable model antiferromagnet. We have chosen it for the following reasons:

- The antiferromagnetic bulk structure of NiO has been well established since the 1960s from extensive neutron and optical studies [10, 11, 13, 50].
- Recent studies on thin films have quantitatively established the angle and temperature dependence of the NiO-XMLD effect [26].
- The AFM-ordered (001) surface can be easily prepared by cleaving single crystals.

NiO grows in a rocksalt structure. The Ni spins are ferromagnetically aligned within {111} sheets that are then antiferromagnetically stacked parallel to a ⟨111⟩ axis, creating a completely compensated bulk structure. Each area of the crystal, exhibiting

one of the four possible ⟨111⟩ stacking directions – [111], [–111], [1–11], [11–1] – is called a T(win)-domain. In each T-domain the easy spin axis can be one of three different ⟨11–2⟩ directions in the ferromagnetically ordered plane. These domains within a T-domain are called (S)pin-domains. We have studied the (001) surface, which is a natural cleavage plane of NiO and corresponds to a plane of compensated spins in the bulk.

2.4.1 Angular Dependence of Domain Contrast in NiO(001)

The angular dependence of the domain contrast provides information about the magnetic symmetry of the surface. Hillebrecht et al. studied the (001) surface of NiO single crystals at about 1 μm spatial resolution using a commercial PEEM at the new BESSY2 synchrotron facility [51]. The results are shown in Fig. 2.8. The XMLD (asymmetry) image was derived from two PEEM images acquired at the main multiplet lines of the NiO L_2 edge, with linear polarization parallel to the sample plane. The black and white stripes in the XMLD image are several μm wide and several 100 μm long and represent two T-domains that are divided by domain walls along the in-plane [100] direction. The image contrast disappears above the bulk Néel temperature of NiO (525 K), confirming its magnetic origin. Several XMLD images were acquired at different azimuthal sample orientations ϕ varying the angle between the X-ray polarization and the in-plane [100] direction of the sample. The variation in the intensity difference or contrast between the black and white domains in these images shows a $\sin(2\phi)$ dependence, which is easily explained by the $\cos^2\phi$ dependence of the XMLD intensity within each domain. From the symmetry of the curve with respect to $\phi = 0$, the authors deduced that the antiferromagnetic structure of the studied NiO(001) surface is symmetric with respect to the (100) domain walls. Furthermore, the amplitude of the curve is a measure of the angle between the magnetic axes.

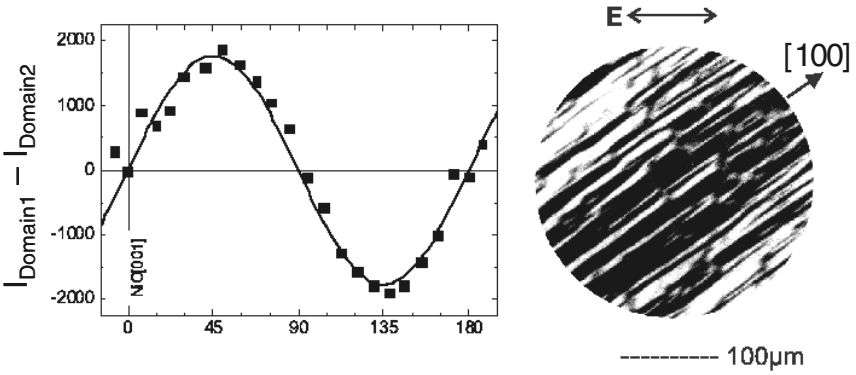

Fig. 2.8. Antiferromagnetic domain pattern on NiO(001) acquired with linear polarization. Black and white areas represent different antiferromagnetic domains, separated by walls parallel to [100]. The intensity difference between black and white domains changes size and sign while rotating the sample around its surface normal, showing a $\sin(2\phi)$ dependence, where ϕ is the angle between the electric field vector and the in-plane [100] direction [51]

2.4.2 Polarization Dependence of Domain Contrast

In the following, we will describe a procedure for the quantitative determination of the orientation of the antiferromagnetic axis within a single domain using spatially resolved spectroscopy (image stacks). This procedure is applicable if the maximum or minimum XMLD effect in an X-ray absorption spectrum of the studied system is known. Since the XMLD effect is superimposed on an isotropic background, which is not known a priori, the experimental spectra need to be compared to reference measurements acquired at perpendicular and parallel alignments of the magnetic axis and the X-ray polarization.

Since the crystallographic symmetry of NiO is known, it is sufficient to search for optimum XMLD contrast with the linear polarization vector aligned with the in-plane projection of the three main symmetry axes of NiO: [100], [110], and [121]. We acquired images and spectra of the same sample area in these three measurement geometries by using linear and "plane" polarization. "Plane" polarization is used synonymously with "circular polarization of either helicity". At the ALS PEEM-2 facility, the degree of circular polarization is about 80%. For plane-polarized radiation, one component of the electric field vector lies in the plane of the sample, and the other lies in the plane of X-ray incidence, tilted by 30° from the surface normal. The second component gives access to the out-of-plane spin component. Note that plane-polarized light can be described by two independent orthogonal electric field vector components. Their relative phase is of no importance in XMLD.

High spatial resolution images for NiO(001), measured with the ALS PEEM-2, are shown in Fig. 2.9. The two images were acquired with linearly (left image) and with plane- (right image) polarized light. The XMLD image acquired with linear polarization shows a distribution of in-plane AFM axes similar to Fig. 2.8, but with improved spatial resolution. Using plane polarization, the out-of-plane component of the spins is revealed. Each antiferromagnetic in-plane domain consists of two classes of domains with different out-of-plane components separated by walls along ⟨110⟩ directions. Because the size of the local XMLD signal is more accurately determined from spectra than from images obtained at a single energy, we acquired image stacks with linear and plane polarization for three different azimuthal sample orientations with the in-plane polarization component parallel to [100], [110], and [120]. The angular dependence of the L_2 XMLD effect then allows the determination of the in-plane antiferromagnetic axis orientation in each domain. In addition, the relative size of the XMLD effect measured with plane and linear polarization is a measure of the inclination angle of the magnetic axis. By comparing these results with spectroscopic measurements by Alders et al. [26] on NiO(001) thin films, we can determine the orientation of the spin axis within each single domain with an accuracy of about $+/-7$ degrees The in-plane component of the orientation of the antiferromagnetic axes is indicated in Fig. 2.9. All four possible T-domains are present, forming a so-called "4-wall" structure. Each T-domain consists of a single ⟨121⟩ S-domain in a configuration that minimizes the magnetic energy of the system. The observed S-domains have their antiferromagnetic axis canted by 35.3° relative to the (001) surface plane. We do not observe any S-domains with a tilt angle of 65.9° from the (001) plane,

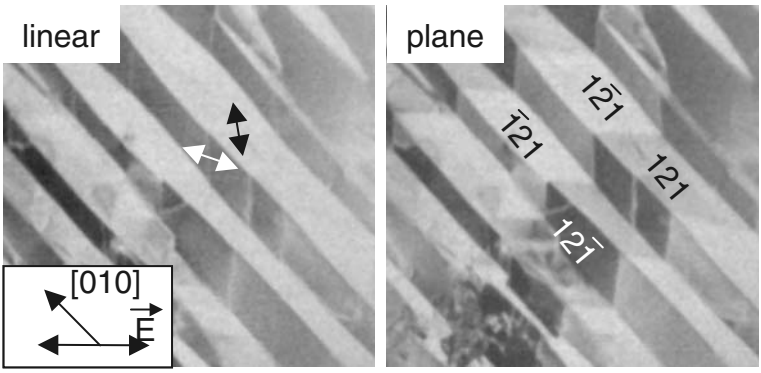

Fig. 2.9. Images of antiferromagnetic domains on NiO(001) acquired with linear (*left*) and plane (*right*) polarization. Using linearly polarized X-rays, two classes of antiferromagnetic domains with different in-plane components of the magnetization are distinguished. Using plane (circularly) polarized X-rays, PEEM becomes sensitive to the out-of-plane component of the magnetic axis, distinguishing four antiferromagnetic T-domains that form a four-wall structure. Arrows and cubic lattice vectors describe the local orientation of the antiferromagnetic axis, derived from a detailed contrast analysis

as are present in the bulk. The breaking of symmetry at the surface, therefore, only supports a subset of all possible bulk antiferromagnetic orientations [10, 11, 13, 50]. Our results demonstrate the capability of polarization and angular-dependent PEEM to determine the orientation of the antiferromagnetic axis at the sample surface in all three dimensions.

2.4.3 Coupling Between Co and NiO–AFM Reorientation

The domain structure of adjacent magnetic layers provides information about the magnetic coupling effects occurring across the interface. We have, therefore, studied the relation of the domain configurations of a 1.5-nm-thick ferromagnetic Co film grown by e-beam evaporation on a NiO(001) substrate [52]. Here, we take advantage of the elemental specificity of X-ray PEEM, which allows the separate investigation of the magnetic properties of the NiO substrate and the Co layer. Taking a close look at the XMLD domain image in Fig. 2.10 (bottom left), which was acquired using plane polarization, we notice that only two AFM domains of the originally four T-domains (top left, before deposition) remain after Co deposition. From this we can conclude that the distribution of the out-of-plane component is now the same in at least two of the four T-domains. A detailed analysis of polarization and angle-dependent images and spectra reveals that the magnetic axis rotates by 35.3° in the (111) plane until it is parallel to either the [110] or [1–10] axis in the (001) surface plane.

The ferromagnetic domain pattern of Co, shown on the right in Fig. 2.10, clearly resembles the antiferromagnetic pattern at the NiO surface. However, we observe four gray levels (black-dark gray-light gray-white), instead of two (darkgray-light gray),

because XMCD distinguishes between ferromagnetic spins that have a projection along (lighter) or opposite to (darker) the photon propagation direction (helicity). The domains (gray) that are nearly perpendicular to the X-ray helicity can also be distinguished in our slightly rotated measurement geometry. Arrows in Fig. 2.10 display the local orientations of the antiferromagnetic axes (double arrows) and the ferromagnetic spin directions (arrows). We observe that the Co and NiO spins are coupled parallel, domain by domain, indicating significant exchange coupling at the interface. This coupling is responsible for a strong, induced in-plane anisotropy of the ferromagnetic layer parallel to the ⟨110⟩ antiferromagnetic spin axes.

The importance of these results is twofold: The rotation of the antiferromagnetic axis after Co deposition signifies that the interfacial Co/NiO structure strongly deviates from the NiO bulk structure, emphasizing the need for surface- and interface-sensitive techniques complementing bulk measurements in order to correctly model the interfacial coupling between ferromagnets and antiferromagnets and to conclu-

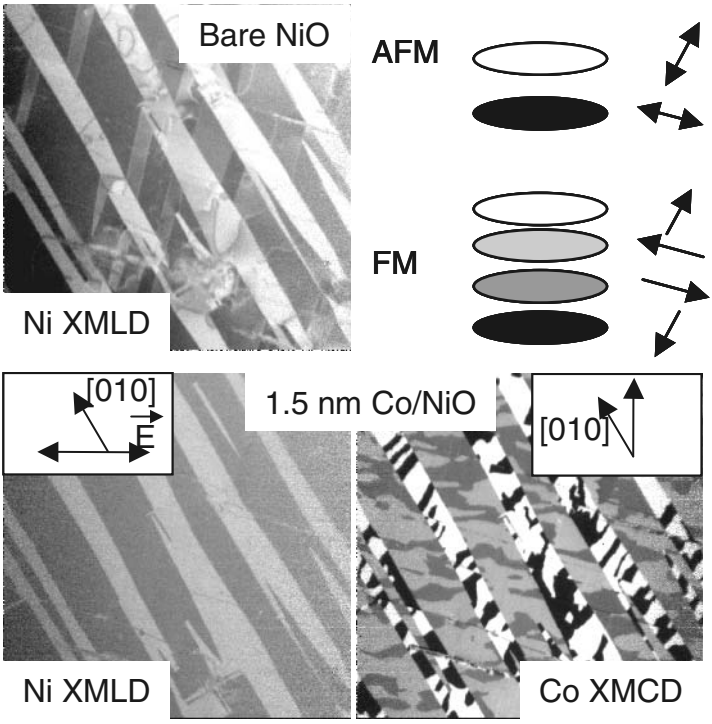

Fig. 2.10. The left column shows XMLD images of NiO(001) before and after Co deposition, recorded with plane polarized X-rays. The original zig-zag pattern of the bare surface visible with plane polarization completely disappears upon Co deposition. The spin axis in the antiferromagnet rotates from [121] toward [110]. Ferromagnetic spins align parallel, domain by domain, to the adjacent antiferromagnetic spins, as indicated in the right image acquired using Co XMCD. Each antiferromagnetic stripe domain breaks up into two ferromagnetic domains with opposite spin directions

sively solve the problem of exchange bias. Furthermore, the measurement reveals that the *parallel* configuration of ferromagnetic and antiferromagnetic spins is the lowest energy state of the system Co/NiO (001). This information is crucial for exchange bias models.

2.4.4 Interfacial Spin Polarization in Co/NiO(001)

After observation of the domain-by-domain coupling across the NiO/Co antiferromagnet-ferromagnet interface, the question arises as to the origin of the coupling. After all, the NiO is supposed to be magnetically neutral! In order to explain exchange coupling and bias, it has long been speculated that the antiferromagnetic interface must contain "uncompensated spins". As described in the Introduction, previous models for their origin involved statistical arguments associated with the termination of bulk antiferromagnetic domains [9], spin-flop canting of antiferromagnetic spins [17], and various defect-based explanations [18, 19]. Here we will discuss PEEM experiments that suggest an altogether different origin of the interfacial spins, namely, the formation of an interfacial layer through chemical reaction. The interfacial layer is shown to create uncompensated spins and to mediate the coupling between the layers [53].

As pointed out in the introduction, the determination of an interface-specific signal is quite challenging, in general. One anticipates only a small concentration of uncompensated interfacial spins of about one monolayer or less. Their signature is superimposed on the large background of the bulk NiO and buried beneath the ferromagnetic Co layer. Our microscopy experiments are aided by recent X-ray absorption experiments on ferromagnet/NiO systems, which revealed chemical oxidation and reduction processes across the interface, leading to the formation of a thin, chemically reacted $CoNiO_x$ layer [37]. We can take advantage of the observed chemical reduction of the NiO layer by tuning the X-ray energy to the maximum of the XMCD effect of Ni metal, thus increasing the sensitivity of PEEM to the interface layer. The moderate surface sensitivity of PEEM, detecting secondary electrons, enhances the strength of the interface signal while retaining the ability to detect a signal from the buried layer.

Our results for the Co/NiO(001) system are shown in Fig. 2.11. Here, the XMCD PEEM image of the ferromagnetic Co film is compared to an XMCD image recorded at the Ni edge. The Ni image was acquired at the metal resonance positions, which are shifted by -0.4 eV compared with the oxide. The Ni XMCD image shows the magnetic structure of *uncompensated* Ni spins that are created at the interface by a chemical reaction of Co with NiO. The images demonstrate a clear correlation of the spin structure of the Co film with that of the $NiCoO_x$ interface layer. This layer is no longer antiferromagnetic, but instead is ferri- or ferromagnetic. The spin contrast in the Ni XMCD image is superimposed on an antiferromagnetic background, caused by the XMLD effect in the antiferromagnet. The thickness of the ferromagnetic layer amounts to 0.5 Å for an as-grown film and increases up to 6 Å after annealing at 600 K, giving rise to an XMCD contrast of 0.3 to 4%. These measurements demonstrate the high sensitivity that can be reached with PEEM, making use of the unique chemical,

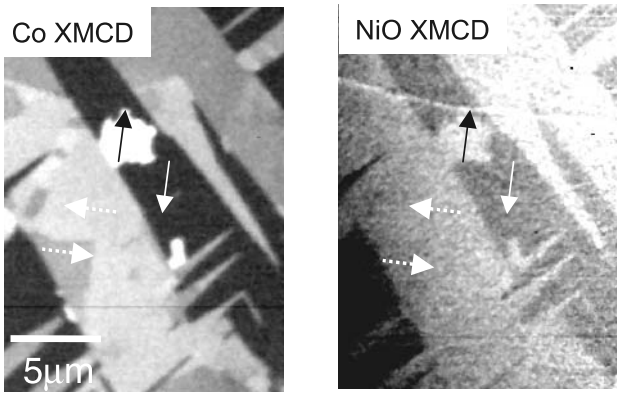

Fig. 2.11. The ferromagnetic domain pattern of Co and the NiO interface are shown using XMCD. Arrows indicate the local direction of the magnetization. The interfacial Ni spin polarization is found to be an exact replica of the ferromagnetic Co domain pattern

elemental, and magnetic specificity of this technique in combination with the surface sensitivity afforded by secondary electron detection. We learn that the chemical reaction at the boundary between an antiferromagnetic oxide and a ferromagnetic metal results in the coupling of the magnetic structures on both sides of the boundary. This first microscopic observation of uncompensated interface spins proves that these spins indeed play an important role in the development of exchange coupling and exchange bias in ferromagnet-antiferromagnet systems.

2.5 Summary

We have demonstrated the power of PEEM to reveal the detailed spin structure near antiferromagnet-ferromagnet interfaces. This capability arises from a unique combination of lateral resolution coupled with elemental, chemical, magnetic, and depth sensitivity. Using this approach, we can pick apart complex magnetic multilayers, one layer at a time, and obtain unprecedented new information on the spin structure near interfaces. The solution of a nearly 50-year-old problem, the microscopic origin of exchange anisotropy, has come within our reach.

The spatial resolution of the PEEM technique can be significantly improved by compensation of the chromatic and spherical image aberrations introduced mostly by the accelerating field and the objective lens. This can be achieved by the introduction of an aberration-correcting electrostatic mirror. Theoretical estimates predict a limit for the spatial resolution of about 1–2 nm [54, 55], which is sufficient for the investigation of typical polycrystalline materials. Two groups, one in the U.S. and one in Germany, are currently designing aberration-corrected instruments that have a design resolution of about 2 nm. These new instruments will be located at BESSY2 (SMART) [54, 55] and the ALS (PEEM-3) [56].

Complementary to the development of higher resolution instruments is the development of higher brightness X-ray sources that provide higher flux and allow tighter focusing of the X-rays. Helical undulators at modern synchrotron facilities are an optimal source for magnetic studies because of their high brightness and control from circular to vertical and horizontal linear polarization. We envision that the combination of ultrahigh resolution PEEM with brilliant insertion device sources will allow access to the full range of nanoscale science, allowing the study of single magnetic grains, clusters, and ultrasmall magnetic patterns. Furthermore, the 50 picosecond X-ray pulse width at modern synchrotron facilities will allow one to explore a time regime in magnetic switching of nanostructures that is presently still a technological dream.

References

1. J.B. Kortright, D.D. Awschalom, J. Stöhr, S.D. Bader, Y.U. Idzerda, S.S.P. Parkin, I.K. Schuller, and H.C. Siegmann, J. Magn. Magn. Mater. **207**, 7 (1999).
2. P.A. Grünberg, Sensors and Actuators A **91**, 153 (2001).
3. G. Prinz, Science **282**, 1660 (1998), G. Prinz, J. Magn. Magn. Mater. **200**, 57 (1999).
4. R. Fiederling, M. Keim, G. Reuscher, W. Ossau, G. Schmidt, A. Waag, and L.W. Molenkamp, Nature **402**, 787 (1999).
5. H. Ohno, Science **281**, 951 (5379).
6. J. Nogues and I.K. Schuller, J. Magn. Magn. Mater. **192**, 203 (1999).
7. A.E. Berkowitz and K.J. Takano, Magn. Magn. Mater. **200**, 552 (1999).
8. W.H. Meiklejohn and C.P. Bean, Phys. Rev. **105**, 904 (1956).
9. K. Takano, R.H. Kodama, A.E. Berkowitz, W. Cao, and G. Thomas, Phys. Rev. Lett. **79**, 1130 (1997).
10. W.L. Roth, J. Appl. Phys. **31**, 2000 (1960).
11. T. Yamada, S. Saito, and Y. Shimomura, J. Phys. Soc. Jpn. **21**, 672 (1966).
12. J. Baruchel, Physica B **192**, 79 (1993).
13. S. Saito, M. Miura, and K. Kurosawa, Journal of Physics. C **13**, 1513 (1980).
14. J. Stöhr, A. Scholl, T.J. Regan, S. Anders, J. Lüning, M.R. Scheinfein, H.A. Padmore, and R.L. White, Phys. Rev. Lett. **83,** 1862 (1999)
15. M. Fiebig, D. Frölich, G. Sluyterman v.L., R.V. Pisarev, Appl. Phys. Lett. **66**, 2906 (1995)
16. M. Fiebig, D. Fröhlich, S. Leute, and R.V. Pisarev, Appl. Phys. B **66**, 265 (1998).
17. N.C. Koon, Phys. Rev. Lett. **78**, 4865 (1997).
18. T.C. Schulthess and W.H. Butler, Phys. Rev. Lett. **81**, 4516 (1998).
19. P. Miltenyi, M. Gierlings, J. Keller, B. Beschoten, G. Güntherodt, U. Nowak, and K.D. Usadel, Phys. Rev. Lett. **84**, 4224 (2000).
20. J. Stöhr, H.A. Padmore, S. Anders, T. Stammler, and M.R. Scheinfein, Surf. Lett. Rev. **5**, 1297 (1998).
21. J. Stöhr and S. Anders, IBM J. Res. Develop. **44**, 535 (2000).
22. B.T. Thole, G. van der Laan, and G.A. Sawatzky, Phys. Rev. Lett. **55**, 2086 (1985).
23. G. van der Laan, B.T. Thole, G.A. Sawatzky, J.B. Goedkoop, J.C. Fuggle, J.-M. Esteva, R. Karnatak, J.P. Remeika, and H.A. Dabkowska, Phys. Rev. B **34**, 6529 (1986).
24. P. Carra, H. Konig, B.T. Thole, and M. Altarelli, Physica B **192**, 182 (1993).
25. P. Kuiper, B.G. Searle, P. Rudolf, L.H. Tjeng, and C.T. Chen, Phys. Rev. Lett. **70**, 1549 (1993).

26. D. Alders, L.H. Tjeng, F.C. Voogt, T. Hibma, G.A. Sawatzky, C.T. Chen, J. Vogel, M. Sacchi, and S. Iacobucci, Phys. Rev. B **57**, 11623 (1998).
27. G. Schütz, W. Wagner, W. Wilhelm, P. Kienle, R. Zeller, R. Frahm, and G. Materlik, Phys. Rev. Lett. **58**, 737 (1987).
28. C.T. Chen, F. Sette, Y. Ma, and S. Modesti, Phys. Rev. B **42**, 7262 (1990).
29. J. Stöhr and R. Nakajima, IBM J. Res. Develop. **42**, 73 (1998).
30. R. Nakajima, J. Stöhr, and Y.U. Idzerda, Phys. Rev. B **59**, 6421 (1999).
31. J. Stöhr, Y. Wu, B.D. Hermsmeier, M.G. Samant, G.R. Harp, S. Koranda, D. Dunham, and B.P. Tonner, Science **259**, 658 (1993).
32. J. Stöhr, "NEXAFS Spectroscopy", Springer Series in Surface Sciences 25, Springer, Berlin (1992).
33. J. Stöhr, J. Magn. Magn. Mat. **200**, 470 (1999).
34. P. Fischer, T. Eimüller, G. Schütz, G. Denbeaux, A. Pearson, L. Johnson, D. Attwood, S. Tsunashima, M. Kumazawa, N. Takagi, M. Kohler, and G. Bayreuther, Rev. Sci. Instrum. **72**, 2322 (2001).
35. D. Attwood, "Soft X-Rays and Extreme Ultraviolet Radiation", Cambridge University Press (2000).
36. S. Anders, H.A. Padmore, R.M. Duarte, T. Renner, Th. Stammler, A. Scholl, M.R. Scheinfein, J. Stöhr, L. Séve, and B. Sinkovic, Rev. Sci. Instrum. **70**, 3973 (1999).
37. T.J. Regan, H. Ohldag, C. Stamm, F. Nolting, J. Lüning, J. Stöhr, and R.L. White, Phys. Rev. B **64**, 214422 (2001).
38. J. Lüning, F. Nolting, H. Ohldag, A. Scholl, E.E. Fullerton, M. Toney, J.W. Seo, J. Fompeyrine, H. Siegwart, J.-P. Locquet, and J. Stöhr, submitted to Phys. Rev. B (2002)
39. A. Scholl, J. Stöhr, J. Lüning, J.W. Seo, J. Fompeyrine, H. Siegwart, J.-P. Locquet, F. Nolting, S. Anders, E.E. Fullerton, M.R. Scheinfein, and H.A. Padmore, Science **287**, 1014 (2000).
40. G. Rempfer and O.H. Griffith, Ultramicroscopy **27**, 273 (1989).
41. B.L. Henke, J.A. Smith, and D.A. Attwood, J. Appl. Phys. **48**, 1852 (1977).
42. E. Bauer, in "Chemical, Structural, and Electronic Analysis of Heterogeneous Surfaces on Nanometer Scale," R. Rosei, Ed., Kluwer Acad. Publ., Dortrecht (1997)
43. G. De Stasio, L. Perfetti, B. Gilbert, O. Fauchoux, M. Capozi, P. Perfetti, G. Margaritondo, and B.P. Tonner, Rev. Sci. Instrum. **70**, 1740 (1999).
44. F. Nolting, A. Scholl, J. Stöhr, J.W. Seo, J. Fompeyrine, H. Siegwart, J.-P. Locquet, S. Anders, J. Lüning, E.E. Fullerton, M.F. Toney, M.R. Scheinfein, and H.A. Padmore, Nature **405**, 767 (2000).
45. D.S. Deng, X.F. Jin and R. Tao, Phys. Rev. B **65**, 132406 (2002).
46. I.M. Lifshitz, Sov. Phys. JETP **15**, 939 (1962).
47. M.M. Farztdinov, Sov. Phys. Usp. **7**, 855 (1965).
48. Y.Y. Li, Phys. Rev. **101**, 1450 (1956).
49. M.M. Farztdinov, Phys. Met. Metall. **19**, 10 (1965).
50. G.A. Slack, J. Appl. Phys. **31**, 1571 (1960).
51. F.U. Hillebrecht, H. Ohldag, N.B. Weber, C. Bethke, U. Mick, M. Weiss, and J. Bahrdt, Phys. Rev. Lett. **86**, 3419 (2001).
52. H. Ohldag, A. Scholl, F. Nolting, S. Anders, F.U. Hillebrecht, and J. Stöhr, Phys. Rev. Lett. **86**, 2878 (2001).
53. H. Ohldag, T.J. Regan, J. Stöhr, A. Scholl, F. Nolting, J. Lüning, C. Stamm, S. Anders, and R.L. White, Phys. Rev. Lett. **87**, 247201 (2001).
54. R. Fink, M.R. Weiss, E. Umbach, D. Preikszas, H. Rose, R. Spehr, P. Hartel, W. Engel, R. Degenhardt, R. Wichtendahl, H. Kuhlenbeck, W. Erlebach, K. Ihmann, R. Schlogl, H.J. Freund, A.M. Bradshaw, G. Lilienkamp, T. Schmidt, E. Bauer, and G. Benner, J. Electron Spectrosc. Relat. Phenom. **84**, 231 (1997).

55. R. Wichtendahl, R. Fink, H. Kuhlenbeck, D. Preikszas, H. Rose, R. Spehr, P. Hartel, W. Engel, R. Schlogl, H.J. Freund, A.M. Bradshaw, G. Lilienkamp, E. Bauer, T. Schmidt, G. Benner, and E. Umbach, Surf. Rev. Lett. **5**, 1249 (1998).
56. J. Feng, H.A. Padmore, D.H. Wei, S. Anders; Y. Wu, A. Scholl, and D. Robin, Rev. Sci. Instrum. **73**, 1514 (2002).